Improving the Accuracy of Stress Intensity Factors Obtained by the Scaled Boundary Finite Element Method on Hierarchical Meshes

***Adrian Egger[1], Savvas Triantafyllou[2], and Eleni Chatzi[1]**

[1]Institute of Structural Engineering, ETH Zurich, Switzerland
[2]Centre for Structural Engineering and Informatics, The University of Nottingham, UK

*Presenting and corresponding author: egger@ibk.baug.ethz.ch

Abstract

In this work, the unique properties of the scaled boundary finite element method (SBFEM), a semi-analytical numerical method, which introduces a scaling center in each element's domain, are exploited to improve the accuracy of computed generalized stress intensity factors (gSIFs) on hybrid balanced quadtree-polygon (QT) meshes. The gSIFs are extracted by harnessing the semi-analytical solution in radial direction. This is achieved by placing the scaling center of the element containing the crack at the crack tip. Taking an analytic limit of this element's stress field as it approaches the crack tip, delivers an expression for the singular stress field. By applying the problem specific boundary conditions, the geometry correction factor is obtained and the gSIFs are then evaluated based on their formal definition.

Computation of the gSIFs by SBFEM permits exceptional accuracy, however, when combined with QT meshes employing linear elements, this does not always hold. Nevertheless, it has been shown that crack propagation schemes are highly effective even given very coarse discretizations, utilizing criteria than only rely on the ratio of mode I to mode II gSIFs. The absolute values of the gSIFs may still be subject to undesirable errors. Hence, we propose a post-processing scheme, which minimizes the error resulting from the approximation space of the cracked element. Thus, the errors in the calculation of the gSIFs is only limited to the discretization error of the quadtree mesh. This is achieved by h- and/or p-refinement of the cracked element, which elevates the amount of modes present in the solution. The resulting numerical description of the element is highly accurate, with the main error source now stemming from its boundary displacement solution. Numerical examples show, that this post-processing procedure can significantly improve the accuracy of the computed gSIFs with negligible computational cost even on coarse meshes resulting from QT decompositions.

Keywords: SBFEM, hierarchial meshes, gSIFs, crack propagation, LEFM.

Introduction

The need for robust, economical and high-fidelity numerical methods to simulate failure processes in linear elastic fracture mechanics (LEFM) arises as as consequence of sustainable design, mandating lighter, stronger and more resilient structures in, e.g., the aerospace, automotive, and construction industries [7, 21, 23]. To this end, several numerical methods have been investigated. Some more notable representatives include: The finite element method, boundary element method, extended finite element method, material point method, meshless methods, peridynamics and recently also the scaled boundary finite element method, which all consider a discrete crack representation. As of late, methods considering diffuse crack representations, e.g., variants of the phase field and thick level set method have been gaining traction, due to their ability to incorporate complex crack behaviour such as nucleation, propagation, branching, merging and arrest [12, 13]. For a comprehensive treatment, we kindly refer the reader to [4].

Although currently the extended finite element method (XFEM) [8] is arguably the most popular method, pending widespread adoption in industry and academia alike, SBFEM [17] offers similar capabilities and additional benefits in LEFM scenarios. SBFEM, which introduces a scaling center within the element domain and, where applicable, at the crack tip, permits an analytic solution in radial direction and thus the gSIFs can be efficiently and effectively evaluated in post-processing as the limit of the singular stress field as one approaches the crack tip [16, 18]. The benefits include the accurate determination of gSIFs at bi-material notches [2] and the fact the no a priori knowledge is required of the order of singularity. Further, SBFEM's polygon underpinning permits direct integration with QT meshes, which eliminates issues with hanging nodes, results in a limited amount of precomputable elements realizations and offers a level of adaptivity around domain features [1, 9, 11, 22].

However, the accurate calculation of gSIFs requires sufficient angular resolution of the singular stress field. This issue is traditionally circumvented by refining an area around the crack tip with subsequent homogenization into a cracked macro element. In conjunction with the balancing operation performed on the QT meshes, this introduces a significant amount of degrees of freedom (DOFs) thus increasing the computational toll of analysis. Although the direction of crack propagation is accurately determined by the ratio of gSIFs, the load-deflection curve can exhibit significant errors. Hence, we aim to increase the accuracy of the calculated gSIFs, utilizing the same global mesh as previously for analysis. This is achieved by enforcing the external boundaries of the cracked element to be compatible with the linear shape functions, yet internally permit the use of arbitrary higher order approximations to model the singular stress field.

This remainder of the paper is structured as follows: First the problem statement and the pertinent theory are summarized. Next, the proposed method is detailed. Subsequently, two numerical examples are investigated. They serve to validate the proposed method and form the basis for the discussion. Finally, conclusions are drawn.

Problem Statement and Pertinent Theory

Problem Statement

To formulate the LEFM problem, we consider a two dimensional cracked domain Ω (Fig. 1). The boundary $\Gamma = \Gamma_0 \cup \Gamma_u \cup \Gamma_t \cup \Gamma_c$ comprises regions of free surface conditions (Γ_0), prescribed displacements $\bar{u}$ (Γ_u) and prescribed traction $\bar{t}$ (Γ_t), where applicable. The strong form with associated boundary conditions follows as:

$$\nabla \cdot \{\sigma\} + \{b\} = \{0\} \qquad \text{in} \quad \Omega \tag{1a}$$

$$\{u\} = \{\bar{u}\} \qquad \text{on} \quad \Gamma_u \tag{1b}$$

$$\{\sigma\} \cdot \{n\} = \{\bar{t}\} \qquad \text{on} \quad \Gamma_t \tag{1c}$$

$$\{\sigma\} \cdot \{n\} = \{0\} \qquad \text{on} \quad \Gamma_c^0 \tag{1d}$$

where $\{\sigma\}$ denotes the Cauchy stress tensor, $\{n\}$ the unit outward normal to the boundary, $\{b\}$ the applied body force per unit volume, $\{u\}$ the displacement field and ∇ the gradient operator.

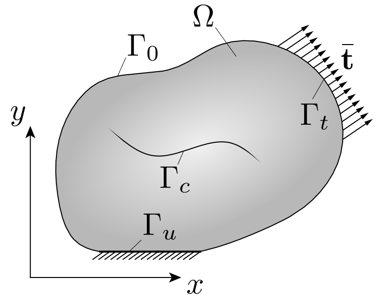

Figure 1: Cracked Body and boundary conditions.

The stress $\{\sigma\}$ and strain field $\{\epsilon\}$, given small deformations and linear elastic material behaviour, follow from the modulus of elasticity E and Poisson ratio ν:

$$\{\epsilon\} = \nabla_s\{u\} \quad \text{and} \quad \{\sigma\} = [D]\{\epsilon\} \tag{2}$$

for which ∇_s is the 2D symmetric gradient operator and $[D]$ the elasticity tensor:

$$[D] = \frac{E}{1-\nu^2}\begin{bmatrix} 1 & \nu & 0 \\ \nu & 1 & 0 \\ 0 & 0 & \dfrac{1-\nu}{2} \end{bmatrix}, \quad \text{for plane stress.} \tag{3}$$

Summary of SBFEM Theory

SBFEM [17] sets itself apart from other numerical methods by the introduction of a scaling center. Only one scaling center may be present per polygonal element, termed a subdomain. One notable restriction is imposed: The complete boundary must be visible from the scaling center, i.e., star-convexity. A new polar-like reference system is introduced with radial coordinate ξ and local tangential coordinate η (Fig. 2).

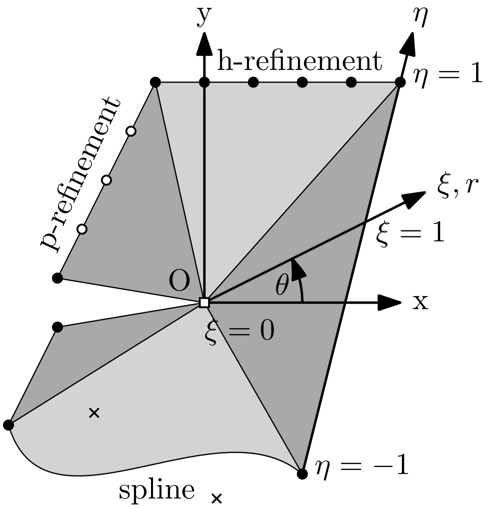

Figure 2: Subdomain with scaled boundary coordinates ξ and η.

The radial coordinate, with origin at the scaling center 0 and a value of 1 on the boundary such that $0 \leq \xi \leq 1$ is kept analytic throughout the analysis. This reduces the dimensionality of the problem by one. In 2D only the boundary remains, which is discretized in the conventional finite element sense, into independent line elements. Each line element possesses its own natural coordinate $-1 < \eta < 1$ in tangential direction. Mapping between

Cartesian (x, y) and scaled boundary coordinates $(x(\xi, \eta), y(\xi, \eta))$ requires an analytic, associated with ξ, and interpolatory, associated with η, component: Any point within the domain can be expressed by scaling of a point $\{x_b\}, \{y_b\}$ on the boundary by a fraction of ξ in radial direction and an interpolation using the conventional finite element shape function $[N(\eta)]$ along the natural coordinate.

$$x(\xi, \eta) = \xi x_b(\eta) = \xi[N(\eta)]\{x_b\} \tag{4}$$

$$y(\xi, \eta) = \xi y_b(\eta) = \xi[N(\eta)]\{y_b\} \tag{5}$$

An iso-parametric representation is adopted and the displacements are analogously mapped:

$$\{u(\xi, \eta)\} = [N_1(\eta)[I], ..., N_n(\eta)[I]]\{u(\xi)\} \tag{6}$$

The amount of degrees of freedom (DOFs) per line element is denoted by n, while $[I]$ is a $2x2$ identity matrix and $\{u(\xi)\}$ represent nodal displacement functions in radial direction, which need to be determined by SBFEM analysis.
Applying the transformation to scaled boundary coordinates, the stresses may be written as [19]:

$$\{\sigma(\xi, \eta)\} = [D]([B^1(\eta)]\{u(\xi)\},_\xi + [B^2(\eta)]\{u(\xi)\}/\xi) \tag{7}$$

where the strain-displacement relation is described by partitioning the linear operator into $[B^1(\eta)]$ and $[B^2(\eta)]$ [17]. Deriving the weak form involves recasting the strong form in scaled boundary coordinates and applying the standard techniques in tangential direction [3, 5, 20]. This gives rise to two equations:

$$[E^0]\xi^2\{u(\xi)\},_{\xi\xi} + ([E^0] - [E^1] + [E^1]^T)\xi\{u(\xi)\},_\xi - [E^2]\{u(\xi)\} = 0 \tag{8}$$

$$\{P\} = [E^0]\xi\{u\},_\xi + [E^1]^T\{u\} \tag{9}$$

The scaled boundary finite element equation in displacements (Eqn. 8) governs the system response within the domain, while Eqn. 9 defines the behavior on the boundary. Three coefficient matrices $[E^0], [E^1], [E^2]$ arise, which bear strong similarity to stiffness matrices in conventional FEM: They are calculated element-wise with subsequent assembly on subdomain level. The vector or nodal forces and displacements on the boundary are given as $\{P\}$ and $\{u\} = \{u(\xi = 1)\}$ respectively. Typically, the solution to the set of homogeneous Euler-Cauchy differential equations is constructed as a power series:

$$\{u(\xi)\} = [\Psi^{(u)}]\xi^{-[S]}\{c\} = \sum_{i=1}^{n}[\Psi_i^{(u)}]\xi^{-[S_i]}\{c_i\} \tag{10}$$

The transformation matrix $[\Psi]$ and block diagonal real Schur form $[S]$ arise from rewritting the quadratic eigen-problem described by combining Eqns. 8 and 9 as a system of first order differential equations:

$$\xi \begin{Bmatrix} \{u(\xi)\} \\ \{q(\xi)\} \end{Bmatrix},_\xi = -[Z] \begin{Bmatrix} \{u(\xi)\} \\ \{q(\xi)\} \end{Bmatrix} \tag{11}$$

with the Hamiltonian coefficient matrix Z defined by

$$Z = \begin{bmatrix} [E^0]^{-1}[E^1]^T & -[E^0]^{-1} \\ -[E^2] + [E^1][E^0]^{-1}[E^1]^T & -[E^1][E^0]^{-1} \end{bmatrix} \tag{12}$$

It can be shown that Eqn. 11 decouples the block-diagonal Schur decomposition [15].

$$[Z][\Psi] = [\Psi][S] \tag{13}$$

The modes comprise the columns of the transformation matrix, while the corresponding eigenvalues are contained within the diagonal blocks of the real Schur form. Having doubled the problem size by considering a system of first order differential equations, the bounded response is striped from the unbounded one by sorting $[S]$ and $[\Psi]$ and partitioning according to sign:

$$[S] = diag([S_{neg}], [S_{pos}]) \tag{14}$$

$$[\Psi] = \begin{bmatrix} [\Psi^{(u)}_{neg} & \Psi^{(u)}_{pos}] \\ [\Psi^{(q)}_{neg} & \Psi^{(q)}_{pos}] \end{bmatrix} \tag{15}$$

Substituting the bounded component of the displacement solution (Eqn. 10) into the equation governing the boundary response (Eqn. 9), the formulation of the subdomain stiffness matrix arises, which permits the calculation of the displacement field using conventional FEM methods.

$$K_{bounded} = [\Psi^{(q)}_{pos}][\Psi^{(u)}_{neg}]^{-1} \tag{16}$$

The final expression of the stresses is obtained by substituting Eqn. 10 into Eqn. 7:

$$\{\sigma(\xi, \eta)\} = \sum_{i=1}^{n} [\Psi_{\sigma i}(\eta)] \xi^{-[S_i]-[I]} \{c_i\}] \tag{17}$$

where stress mode $[\Psi_{\sigma i}(\eta)]$ arise from its corresponding displacement mode $[\Psi^{(u)}_i]$:

$$[\Psi_{\sigma i}(\eta)] = [D](-[B^1(\eta)][\Psi^{(u)}_i][S_i] + [B^2(\eta)][\Psi^{(u)}_i]) \tag{18}$$

Generalized Stress Intensity Factors

Since the general solution to the SBFEM equation is constructed from a power series, the singular modes are readily identified: By inspection of S_i, any $-1 < real(\lambda) < 0$ will result in a singularity at $\xi = 0$. By placing the scaling center at a crack tip, this feature is exploited in calculating the gSIFs (Fig. 2). By including a double node at the crack mouth, two additional modes, i.e., the singular modes, arise, whose eigen-vectors resemble the mode I and mode II fracture cases. The singular stress field is extracted from the general solution (Eqn. 17), where the superscript $^{(s)}$ denotes the singular quantities:

$$\{\sigma^{(s)}(\xi, \eta)\} = [\Psi^{(s)}_{\sigma}(\eta)] \xi^{-([S^{(s)}]-[I])} \{c^{(s)}\} \tag{19}$$

Only the components $\{\sigma^{(s)}(r, \theta)\} = (\sigma^{(s)}_{\theta}(r, \theta), \tau^{(s)}_{r\theta}(r, \theta))^T$ are retained, which correspond to mode I and II cracks.

$$\begin{Bmatrix} \sigma^{(s)}_{\theta}(r, \theta) \\ \tau^{(s)}_{r\theta}(r, \theta) \end{Bmatrix} = \frac{1}{\sqrt{2\pi L}} \xi^{-[\tilde{S}^{(s)}(\theta)]} \begin{Bmatrix} K_I(\theta) \\ K_{II}(\theta) \end{Bmatrix} \tag{20}$$

Comparing Eqn. 20 to the gSIFs formal definition [18] permits their evaluation as:

$$\begin{Bmatrix} K_I(\theta) \\ K_{II}(\theta) \end{Bmatrix} = \sqrt{2\pi L} \{\sigma^{(s)}\} \tag{21}$$

Hierarchical Meshes

Hierarchical meshes arising from quadtree decompositions traditionally suffer from hanging nodes, whose treatment typically incurs computational, algorithmic or implementational overhead. Leveraging the polygon-underpinnings of SBFEM alleviates all issues commonly associated with hanging nodes, resulting in analysis ready meshes. To avoid irregularity of the mesh, a balancing operation is performed, which limits the amount of unique subdomain realization to 16 and enables precomputation. Hence, this approach garners considerable attention [1, 10, 11].
Strong and weak discontinuities are introduced by clipping the QT mesh [9]. Contrary to the XFEM, double nodes are introduced. Crack tips require special treatment: A double node is introduced where the crack enters an element and the scaling center is placed at the crack tip (Fig. 2). Crack tips do not require discretization, however, they are assumed straight. For crack propagation calculations, sufficiently accurate SIFs are required. Unfortunately, the elements typically encountered on QT meshes do not permit sufficient resolution of the singular stress field. Hence, a region around the crack tip is first locally refined and then homogenized (Fig. 3, bottom left). Imposing a suitable criteria to determine the critical crack propagation angle in conjunction with a user specified crack propagation increment Δa, determines the crack tip location in the subsequent step (Fig. 3, bottom right). Due to the balancing operation, the homogenization step affects large portions of the mesh, introduces many spurious DOFs in the process and forces a substantial system update across iterations. The increased accuracy with which the SIFs are calculated is attributed to two affects: Mesh refinement about the singularity and improving the approximation space of the crack tip element.

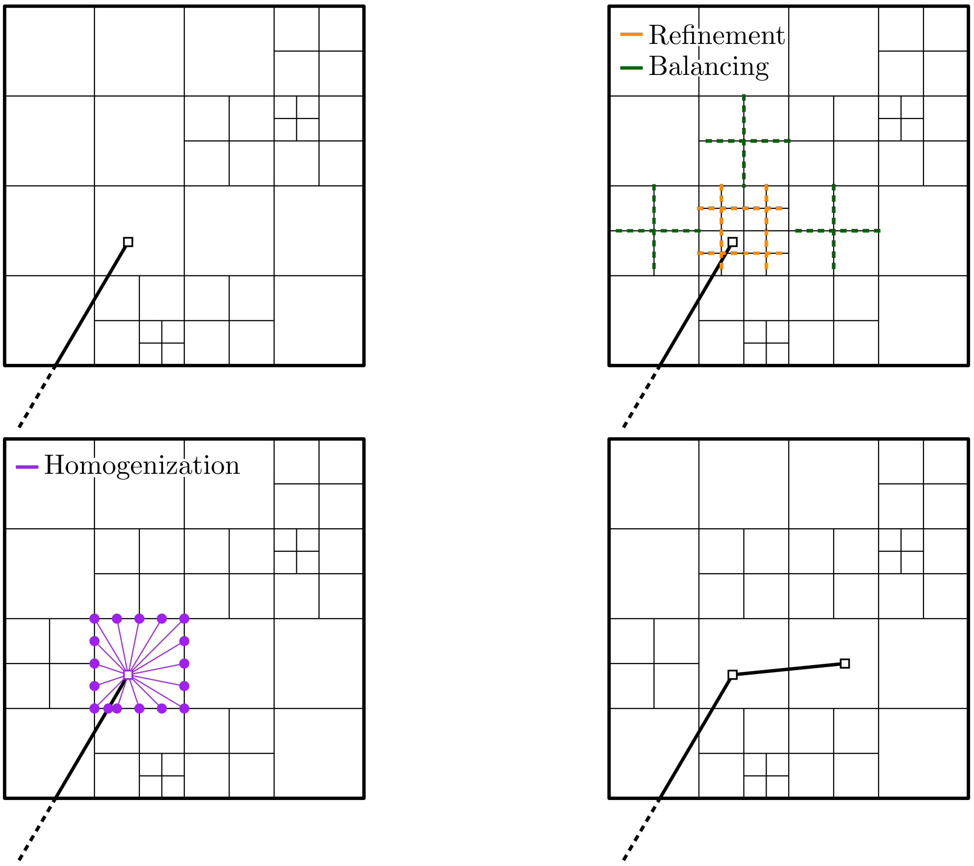

Figure 3: Stages in crack propagation by SBFEM on QT meshes.

Proposed Method

By inspecting the expression of the singular stresses (Eqn. 19), the accuracy of the gSIFs (Eqn. 21) can be improved in two ways:

1. Finding a better approximation for the integration constants $[c]$ stemming from the displacement solution of the domain.
2. Enhancing the displacement and thus stress field approximation $[\Psi]$ and $[S]$ within the cracked element by escalating the amount of DOFs present.

The contribution of the first source can be adjusted by h- or p-refinement on the mesh, either locally or globally. However, this is a costly procedure due to, e.g., remeshing, reassembly followed by solution, in the understanding that a significant amount of DOFs are newly introduced. Considering the convergence rate of the linear elements employed, this is deemed a sub-optimal approach from a computational resources standpoint. The second source allows for enhancement directly in post-processing and permits certain insight into how close we might be to the exact solution, by contrasting the gSIFs calculated using the traditional approach to those using the improved scheme.
The steps comprising the improved scheme are:

1. **Perform analysis**
   A displacement solution for the given mesh is sought.
2. **Create a high order cracked element**
   The existing cracked element is replaced by one elevated by h- and/or p-refinement. New nodes, lying in-between existing QT mesh nodes, are introduced in the process.
3. **Impose linearized displacements on all DOFs**
   To guarantee compatibility with the surrounding QT mesh, linear displacements are enforced between its nodes, on the boundary of the elevated cracked element.
4. **Back calculate $[c]$ for cracked element**
   Since the cracked element comprises one subdomain, with all DOFs situated on the boundary, where the prescribed displacements are imposed, the calculation of the stiffness matrix is not necessary. Only the block-diagonal Schur decomposition is required. The integration constants are obtained as $[c] = [\Psi^{(u)}_{neg}]^{-1}\{u\}$ [17]. Typically, refined crack elements comprising 100 DOFs have sufficiently converged. Since the original already contains 10-30 DOFs, this does not noticeably impact computation time.
5. **Extract singular stress modes**
   The identification and extraction of the singular stress modes remains unchanged.
6. **Calculate gSIFs**
   The gSIFs are calculated given Eqn. 21, however, now based on the quantities originating from the elevated cracked element.
7. **Contrast original with improved gSIFs**
   By contrasting the values for the gSIFs calculated by both methods, we can gauge the quality of the original analysis. If the discrepancy in gSIFs is deemed too large, refinement of the original mesh may be warranted.

Numerical Examples

Edge cracked square plate in mode II

An edge cracked square plate subjected to a plane stress state is examined (Fig. 4). Along the boundary, the analytic solution [6] of the near-tip crack field is prescribed given $K_{II} = 1$ (Tab. 1), imposing pure mode II loading. The material properties are $E = 200$ [N/mm^2], $v = 0.3$ and the side length is $L = 1$ [mm].

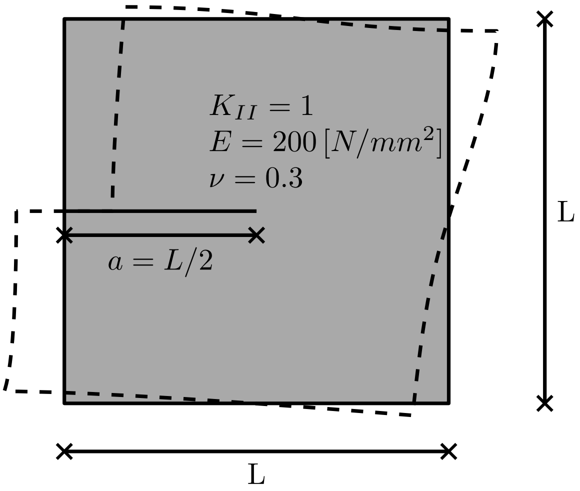

Figure 4: Experimental setup for numerical example A.

Table 1: Analytic solution of the near-tip crack field.

	Exact displacement solution for mode II fracture
u_x	$\frac{K_{II}}{2\mu}\sqrt{r/(2\pi)}sin\frac{\theta}{2}\left(\kappa + 1 + 2cos^2\frac{\theta}{2}\right)$
u_y	$-\frac{K_{II}}{2\mu}\sqrt{r/(2\pi)}cos\frac{\theta}{2}\left(\kappa - 1 - 2sin^2\frac{\theta}{2}\right)$

Three cracked element discretizations are considered, as they arise typically on QT meshes, prior to the refinement and homogenization steps (Fig. 3). The exact solution is applied to the QT mesh nodes identified in Fig. 5. The remaining nodes resulting from internal element refinement are restricted to move as a linear combination of their neighbouring QT mesh nodes, enforcing compatibility.

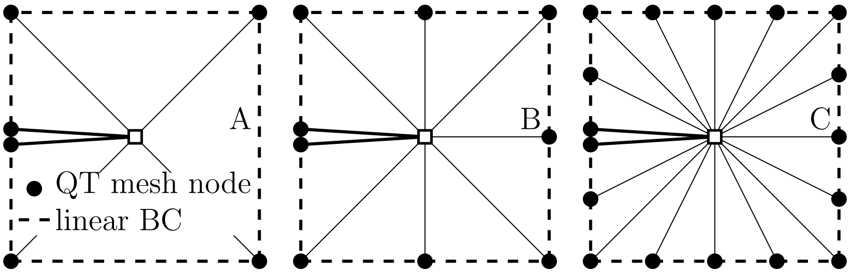

Figure 5: Typical element types A-C arising from QT meshes.

The convergence behaviour is investigated in Fig. 6. Due to the over-constraining of the boundary, deviation in convergence behaviour is expected, i.e., by enforcing linearly

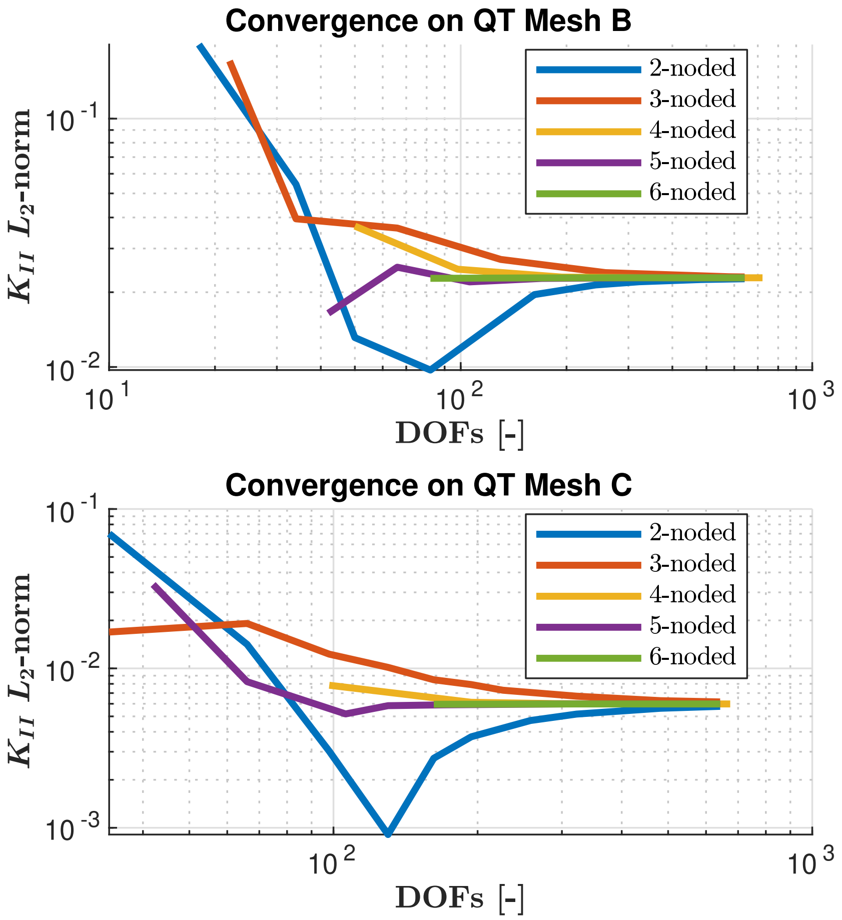

Figure 6: Convergence behaviour of K_{II} on QT meshes employing n-noded elements as boundary discretization.

dependant displacement boundary conditions between QT mesh nodes, an effective stress state is imposed that differs mildly from the exact solution. In this example, the gSIFs are therefore slightly overestimated, which is evident in the asymptotic behaviour on all three meshes. Nevertheless, the error in K_{II} is significantly reduced for all QT meshes, as can be seen in Tab. 2. The diverging results for the case of 2-noded elements is explained by the examination of the absolute values. While the higher order elements approach the asymptotic solution from the high end, the two-noded elements approach from the lower end, thus crossing the imposed $K_{II} = 1$ in the process. The obtainable accuracy is naturally limited to the asymptotic case by the artificially imposed boundary conditions. Therefore, the expected convergence behaviour is disrupted accordingly. In this specific example, the convergence behaviour of even-noded elements was observed to behave predictably, while the odd-noded elements exhibited slight oscillatory behaviour. It can be observed that the computed values for K_{II} remain practically stable when more than 100 DOFs are employed within the cracked element. Preference should be given to higher order elements due to their enhanced convergence properties. On a contemporary laptop employing unoptimized Matlab code, this entails calculations completing in less than 0.1s. Tab. 2 provides the results for K_{II} calculated on the original QT meshes and contrasts them to the asymptotic solutions for the refined crack elements, given a high fidelity SBFEM solution. Assuming a user-specified accuracy tolerance, the improved method of calculating the gSIFs facilitates a decision criterion on whether global mesh refinement is required. The difference in achieved accuracy for each QT mesh is primarily attributed to the manner in which the enforced displacements on the boundary conform to the exact field solution. Deviations therein are reflected in the integration constants $[c]$ (Eqn. 19) and comprise the remaining error in the asymptotic solution. In a practical application of this method, the displacement solution on the QT mesh nodes results from the FEM solution of the global QT mesh. Since the method proposed to improve the calculation of gSIFs does not increase the amount of global DOFs, the overall analysis does not differ. Solely on the cracked element that is refined, "virtual" nodes are introduced that, however, never manifest in calculation of system displacements as their values are predetermined due to the linearized BCs. In principle, a more accurate representation of the displacement modes and eigenvalues is achieved inside the cracked element, while the boundary constraints remain unchanged. This explains the counter intuitive results of the asymptotic error for QT mesh type A for which smaller errors are observed than for the QT mesh type B: For this specific loading, i.e., mode II excitation, on average, the enforced displacement field on the boundary results in a closer approximation of the exact stress field. If mode I excitation where, however, considered, for which the right boundary of the cracked element exhibits concave behaviour, QT mesh Type A results in a 15% error, since it is not able to reproduce such displacement behaviour. Between QT meshes type B and C we observe convergence as expected, as QT mesh C can represent all displacement modes of QT mesh B, while also introducing additional ones.

Table 2: Convergence of gSIFs to imposed solution.

Method		K_{II}	**error [-]**	**error [%]**
imposed		1	-	-
(v) hi-fi		1.00000000524414	≈ 0	≈ 0
(iii) QT mesh	A	1.01547261490198	0.0155	1.55
	B	0.80116357970950	0.1988	19.88
	C	0.92998436271287	0.0700	7.00
(iv) asympt.	A	1.011248626117779	0.0113	1.12
	B	1.02286467268900	0.0287	2.29
	C	1.00598223218854	0.0060	0.60

Edge cracked square plate in mode I

An edge cracked square plate subject to a plane stress state is examined (Fig. 7). The bottom edge of the plate is fully clamped, while on the top edge forced displacements $u_y = 1$ and $u_x = 0$ are applied. The Young's modulus, Poisson's ratio, fracture energy, crack propagation increment and side length are given as $E = 200$ [N/mm^2], $v = 0.3$, $G_c = 2.7$ [N/mm^2], $\Delta a = 0.025$ [mm] and $L = 1$ [mm] respectively.

First, the load-deflection curves obtained from several methods are compared: (i) XFEM, (ii) traditional QT SBFEM, (iii) SBFEM on QT mesh types A-C, (iv) the newly proposed SBFEM method and (v) a high fidelity SBFEM solution comprising one subdomain with h- and p-refinement. The load-deflection curves (Fig. 8) are constructed using the following procedure:

1. Calculate the critical stress intensity factor K_c from the E-modulus and the critical

energy release rate G_c:

$$K_c = \sqrt{EG_c} \quad \text{for plane stress} \tag{22}$$

2. Formulate the equivalent stress intensity factor K_{eq}:

$$K_{eq} = \sqrt{K_I^2 + K_{II}^2} \tag{23}$$

   This implies that the crack propagates as soon as $K_{eq} \leq K_c$. Hence, the gSIFs and the sum of the reaction forces are stored at each iteration.

3. Determine the load factor such that crack propagation initiates, i.e., as the ratio K_c/K_{eq}. The effective displacements and loads at each crack increment step are calculated by scaling the initially imposed values by the load factor.

4. Employ the minimum strain energy density criterion (or equivalent) to calculate the crack propagation angle [14]:

$$\theta_c = 2\tan^{-1}\left[\frac{-2K_I/K_{II}}{1+\sqrt{1+8(K_I/K_{II})^2}}\right] \tag{24}$$

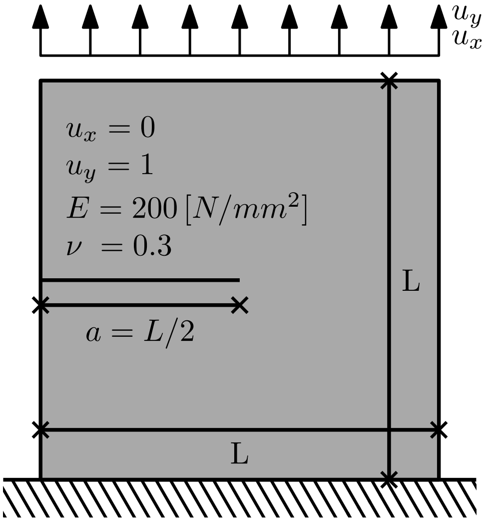

Figure 7: Experimental setup for numerical example A.

For this simple example, the crack paths for all methods coincide, i.e., they propagate in direct extension of the imposed crack. Investigating the load-deflection behaviour (Fig. 8), two reference solutions are constructed: a high fidelity SBFEM solution (v) employing 568 DOFs and an XFEM solution (i) employing a domain discretization of 161x161 element (52'488 DOFs). As expected, the traditional approach (ii) utilizing 1024 DOFs mirrors the reference XFEM solution. Similarly, the correct load-deflection response is obtained by the novel approach (iv), however, employing only 880 DOFs, i.e., on the same mesh as the deficient method (iii). The difference in DOFs is attributed to the balancing operation following refinement around the crack tip, which propagates across the domain.
Given this specific geometry, an exact solution for the crack tip singularity is available, i.e., a square root singularity, which we exploit for benchmarking purposes. By inspection

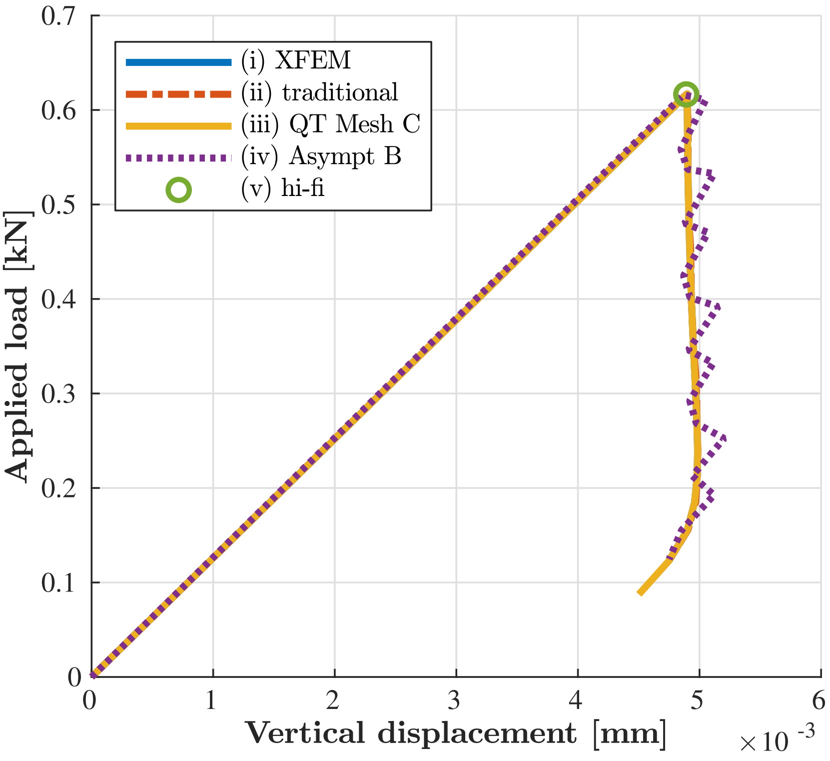

Figure 8: Load deflection curves for methods (i) - (v).

of Eqn. 19, this is the case when all eigenvalues contained in $[S^{(s)}]$ are equal to 0.5. Since the singular eigenvalues depend only on the boundary discretization, a SBFEM element's ability to reproduce the exact solution is purely a reflection of its approximation space. Hence, by leveraging hp-elements, the error in calculated gSIFs, due to the choice of approximation space, can be minimized so that the remaining error stems only from the surrounding mesh discretization. Tab. 3 summarizes the results for the SBFEM based methods given different levels of refinement. As expected, the hi-fi (v) solution is able to approximate the exact solution to nearly machine precision even with very few DOFs. Both the proposed method (iv) and traditional (ii) approaches deliver approximations accurate to several significant figures. For method (iv) 3- and 5-noded elements, denoted by 3n and 5n respectively are considered. For method (ii), studies were conducted using either {2,3,6,12} linear elements per long side of the cracked domain. It can be observed that the proposed method (iv) significantly outperforms the traditional (ii) approach at similar internal discretization levels. The elements, as they are employed in method (iii), perform poorly and report significantly fewer accurate digits.

We compare K_I obtained by our proposed method (iv) and method (iii) to the hi-fi reference solution (v) (Tab. 4). Since both methods employ the same mesh, we isolate the gains of proposed method (iv). Indeed, for mesh types A and B we observe an improvement in accuracy of the calculated gSIFs by approximately and order of magnitude. For mesh C, however, we approach a limit given by the discretization error of the underlying mesh and therefore the error cannot be reduced to such a degrees as with the previous meshes. Nevertheless, accuracy $< 1\%$ is readily achieved, indicating a sufficiently accurate solution for most SIF-based applications.

Table 3: Convergence of eigenvalues to square root singularity.

Method		DOFs	$\boldsymbol{\lambda_1}$	$\boldsymbol{\lambda_2}$
exact		-	0.5	0.5
(ii) trad.	2	34	0.502106496308655	0.502106496308665
	3	66	0.500547555626861	0.500547555626900
	6	162	0.500088619101087	0.500088619101087
	12	322	0.500022191325667	0.500022191325716
(iii) QT mesh	A	12	0.543331260622274	0.487073508787698
	B	18	0.506300843546734	0.506300843547260
	C	34	0.501432879576478	0.501432879577241
(iv) asympt.	3n	66	0.499993111156218	0.499991972174270
	3n	98	0.499998547338467	0.499998547338467
	3n	130	0.499999524753473	0.499999524753473
	5n	42	0.500958236174165	0.500555777249317
	5n	68	0.500001822342609	0.500001760606780
	5n	106	0.500000389900685	0.500000214938575
(v) hi-fi		578	0.499999999998063	0.500000000000369

Table 4: Convergence of gSIFs to high-fidelity solution.

Method		$\boldsymbol{K_I}$	error [-]	error [%]
(iii) QT mesh	A	18.824826991544300	3.4427	22.38
	B	17.144699325716516	1.7626	11.46
	C	15.767196554450349	0.3851	2.50
(iv) asympt.	A	15.714940415023673	0.3328	2.16
	B	15.629945166079814	0.2478	1.61
	C	15.457607616329554	0.0755	0.49
(v) hi-fi		15.382113483624098	-	-

Conclusion

This paper demonstrates that the accuracy of gSIFs calculated on hierarchical meshes can be significantly enhanced by implementing local refinement of the cracked element, while constraining the boundary displacements to conform with the surrounding mesh. The error stemming from the element's ability to accurately represent the singular stress field is alleviated and the remaining deviation is attributed to the discretization error introduced by the mesh. The proposed method permits the use of significantly coarse discretizations of the domain without the need for artificial refinement about the crack tip to obtain comparable accuracy of the gSIFs. This benefit is compounded, since the balancing operation employed on the hierarchical mesh, to arrive at a finite number of precomputable element realizations, is eliminated. Numerical examples have demonstrated that the use of higher order elements and approximately 100 DOFs in the refined element produce accurate results, while retaining high computational efficiency. The limitations of this approach stem from the linear boundary discretization, imposing artificial constraints on the solution. The use of higher order elements, such as cubic line elements on hierarchical meshes could minimize this issue and require the development of targeted implementations for more involved domain geometries.

Acknowledgment

This research was performed under the auspices of the Swiss National Science Foundation (SNSF), Grant # 200021_153379, A Multiscale Hysteretic XFEM Scheme for the Analysis of Composite Structures. The authors would like to thank the group of Prof. Song from UNSW for guidance and code on SBFEM. Further, we would like to extend our thanks to Prof. Devloo from UNICAMP for his illuminating discussions. Finally, we extend our gratitude to Dr. Agathos for allowing access to his XFEM codes.

References

[1] Chen, X., Luo, T., Ooi, E., Ooi, E., and Song, C. A quadtree-polygon-based scaled boundary finite element method for crack propagation modeling in functionally graded materials. *Theoretical and Applied Fracture Mechanics 94* (apr 2018), 120–133.

[2] Chowdhury, M. S., Song, C., and Gao, W. Highly accurate solutions and Pad approximants of the stress intensity factors and T-stress for standard specimens. *Engineering Fracture Mechanics 144* (aug 2015), 46–67.

[3] Deeks, A. J., and Wolf, J. P. A virtual work derivation of the scaled boundary finite-element method for elastostatics. *Computational Mechanics 28*, 6 (jun 2002), 489–504.

[4] Egger, A., Pillai, U., Agathos, K., Kakouris, E., Chatzi, E., Aschroft, I. A., and Triantafyllou, S. P. Discrete and phase field methods for linear elastic fracture mechanics: A comparative study and state-of-the-art review. *Applied Sciences 9*, 12 (June 2019), 2436.

[5] Hu, Z., Lin, G., Wang, Y., and Liu, J. A Hamiltonian-based derivation of Scaled Boundary Finite Element Method for elasticity problems. *IOP Conference Series: Materials Science and Engineering 10* (jun 2010), 012213.

[6] Janssen, M. *Fracture mechanics*. DUP Blue Print, Delft, 2002.

[7] Liu, P., and Zheng, J. Recent developments on damage modeling and finite element analysis for composite laminates: a review. *Materials & Design 31*, 8 (2010), 3825–3834.

[8] Mos, N., Dolbow, J., and Belytschko, T. A finite element method for crack growth without remeshing. *International Journal for Numerical Methods in Engineering 46*, 1 (Sept. 1999), 131–150.

[9] Ooi, E., Man, H., Natarajan, S., and Song, C. Adaptation of quadtree meshes in the scaled boundary finite element method for crack propagation modelling. *Engineering Fracture Mechanics 144* (aug 2015), 101–117.

[10] Ooi, E. T., Natarajan, S., Song, C., and Ooi, E. H. Dynamic fracture simulations using the scaled boundary finite element method on hybrid polygonquadtree meshes. *International Journal of Impact Engineering 90* (apr 2016), 154–164.

[11] Ooi, E. T., Natarajan, S., Song, C., and Ooi, E. H. Crack propagation modelling in concrete using the scaled boundary finite element method with hybrid polygonquadtree meshes. *International Journal of Fracture 203*, 1-2 (jan 2017), 135–157.

[12] Ravi-Chandar, K. Dynamic fracture of nominally brittle materials. *International Journal of Fracture 90*, 1-2 (1998), 83–102.

[13] Ravi-Chandar, K., and Knauss, W. An experimental investigation into dynamic fracture: Iii. on steady-state crack propagation and crack branching. *International Journal of fracture 26*, 2 (1984), 141–154.

[14] Sih, G. Strain-energy-density factor applied to mixed mode crack problems. *International Journal of fracture 10*, 3 (1974), 305–321.

[15] Song, C. A matrix function solution for the scaled boundary finite-element equation in statics. *Computer Methods in Applied Mechanics and Engineering 193*, 23-26 (jun 2004), 2325–2356.

[16] Song, C. Evaluation of power-logarithmic singularities, T-stresses and higher order terms of in-plane singular stress fields at cracks and multi-material corners. *Engineering Fracture Mechanics 72*, 10 (July 2005), 1498–1530.

[17] Song, C. *The scaled boundary finite element method: intorduction to theory and implementation.* John Wiley & Sons, Hoboken, New Jersey, 2018.

[18] Song, C., Tin-Loi, F., and Gao, W. A definition and evaluation procedure of generalized stress intensity factors at cracks and multi-material wedges. *Engineering Fracture Mechanics 77*, 12 (aug 2010), 2316–2336.

[19] Song, C., and Wolf, J. P. The scaled boundary finite-element methodalias consistent infinitesimal finite-element cell methodfor elastodynamics. *Computer Methods in Applied Mechanics and Engineering 147*, 3-4 (aug 1997), 329–355.

[20] Wolf, J. P. *The scaled boundary finite element method.* J. Wiley, Chichester, West Sussex, England ; Hoboken, NJ, USA, 2003.

[21] Xu, P., Zheng, J., and Liu, P. Finite element analysis of burst pressure of composite hydrogen storage vessels. *Materials & Design 30*, 7 (2009), 2295–2301.

[22] Yang, Z. Fully automatic modelling of mixed-mode crack propagation using scaled boundary finite element method. *Engineering Fracture Mechanics 73*, 12 (aug 2006), 1711–1731.

[23] Zheng, J., and Liu, P. Elasto-plastic stress analysis and burst strength evaluation of al-carbon fiber/epoxy composite cylindrical laminates. *Computational Materials Science 42*, 3 (2008), 453–461.